



# Automated processing of planetary hyperspectral datasets for the extraction of weak mineral signatures and applications to CRISM observations of hydrated silicates on Mars

J. Carter <sup>a,b,\*</sup>, F. Poulet <sup>b</sup>, S. Murchie <sup>c</sup>, J.P. Bibring <sup>b</sup>

<sup>a</sup> European Southern Observatory, Vitacura, Santiago, Chile

<sup>b</sup> Institut d'Astrophysique Spatiale, Bat 121, Université Paris-Sud, Orsay, France

<sup>c</sup> Applied Physics Laboratory, Laurel, MD 20723, USA

## ARTICLE INFO

### Article history:

Received 28 June 2012

Accepted 19 November 2012

Available online 1 December 2012

### Keywords:

CRISM

Mars

Hydrated minerals

Epidote

Remote sensing

VNIR reflectance spectroscopy

## ABSTRACT

Near infrared imaging spectrometers are key tools to investigate planetary surfaces in the Solar System. By coupling spectral and spatial information, they give access to the composition and morphology of the planets' surfaces which in turn provide insight into the geological state and history of the body. Processing and interpreting their datasets is however challenging owing to the very large amount of data they produce, a small subset of which contain relevant information, but also to numerous sources of errors, due to the instruments themselves or to observational biases, which further complicate the extraction of interesting but subtle spectral features. Collectively, these limitations have motivated the development of a set of tools that tackle these issues to facilitate the extraction of mineralogical information. The tools described here are successfully applied to the CRISM imaging spectrometer orbiting Mars in the search for hydrated silicates. An automated extraction of the hydrated silica signatures is performed at high accuracy and the discovery of a new mineral on Mars, epidote, is reported thanks to these new data reduction and analysis strategies.

© 2012 Elsevier Ltd. All rights reserved.

## 1. Introduction

### 1.1. Hyperspectral observations of planetary surfaces

Imaging spectrometers are amongst the best tools to investigate the composition of planetary surfaces and atmospheres, and their high science return has resulted in having these instruments as part of the payload in a number of current and planned planetary missions. Although these instruments commonly produce data having lower spectral resolution ( $R_{2\text{ }\mu\text{m}} \leq 500$ ) and higher detector noise levels than their ground-based telescopic counterparts, they offer unrivalled spatial resolution which is paramount when investigating the mineralogical and morphological diversity on any planetary surface. On Mars, for example, the OMEGA/Mars Express instrument allowed the first identification of hydrated clays (Poulet et al., 2005). On Europa, the NIMS/Galileo instrument allowed the identification of hydrated sulphates and sulphuric acid (McCord et al., 1998). On Titan, the

VIMS/Cassini instrument identified hydrocarbon lakes and clouds (Brown et al., 2008).

Despite the high spatial resolution of spacecraft-mounted imaging spectrometers (resolution is  $\sim 18\text{ m/pixel}$  at best using the CRISM/MRO instrument orbiting Mars), these instruments sometimes fail to detect small outcrops due to instrument artefacts and noise, observational biases such as aerosols, atmospheric and photometric effects (e.g. shadows), and mixtures with other minerals. Collectively, all these factors can lead to a significant under-estimation of the amount, extent, and diversity of mineral groups having weak spectral signatures. Additionally, a manual investigation of entire hyperspectral datasets is not feasible given the large amount of data to process (e.g. CRISM high-resolution observations contain about  $6 \times 10^9$  spectra). These limitations on data from imaging spectrometer can be addressed with new processing methods.

A number of methods have been derived over the years to detect, map and identify minerals on planetary surfaces. The most classical approach which has been utilized since the advent of spectral imaging is to detect and map minerals based on simple arithmetic between spectral channels (spectels). By comparing the surface reflectance value between the side(s) and centre of an absorption feature, it is possible to test its presence and assess its depth (Clark and Roush, 1984). Each arithmetic function is tuned

\* Corresponding author at: European Southern Observatory, Vitacura, Santiago, Chile. Tel.: +56 990 063 822.

E-mail address: jcarter@eso.org (J. Carter).

to a specific absorption feature which is then mapped with the imaging spectrometers. These spectral ‘indices’, ‘parameters’, or ‘summary products’ (we will use the term ‘parameter’ hereafter) are a supervised classification method. By merging these maps it is possible to further discriminate the minerals so far as broad families (e.g. Pelkey et al., 2007 in the case of hydrated minerals).

Due to the complexity of building synthetic theoretical spectra of certain minerals (e.g. Balan et al., 2002) but also due to the large number of degrees of freedom in the cation composition (both structural and inter-layer for hydrated minerals) which have an impact on the spectra, final identification of minerals always resorts to comparison with laboratory spectra of Earth-analogues. Spectral repositories of NIR reflectance spectra have been built over the years and provide a very extensive and diverse sample of minerals for comparison (e.g. the NASA/RELAB and USGS spectral libraries: Clark, 2007; Pieters, 2010). Either a visual inspection or a mathematical comparison of the laboratory and measured planetary spectra is carried out. Although efficient for the detection of large, multi-pixel exposures within a few observations, this approach is manually tedious and labour intensive, as well as unsuitable for very weak signatures in the case of a low signal-to-noise data.

Numerous alternatives exist, the most promising being based on an unsupervised blind source separation. Opposite to the supervised method, the spectral information of each observation is classified based on statistical or geometrical criteria with little to no input from the user. Principal component analysis (PCA) is a common example in which the hyperspectral data cube ( $X, Y, \lambda$ ) is projected on a new orthogonal base that better represents the spectral variance in the data. The data cube is no longer a stack of images at different spectral channels but is transformed into a stack of layers ordered by decreasing variance. This approach also reduces the dimensionality of the data as only the first few layers typically have any meaningful information. The first few corresponding eigenvectors of the PCA transform can then be mathematically compared to laboratory spectra to attempt an unsupervised classification of the spectral content within each observation. This type of approach does not require prior knowledge of the spectral features and is usually deemed more appropriate to explore datasets in the search of new mineral phases. A major drawback of this method however is that interesting but subtle spectral features may be lost while systematic spectral artefacts are kept. Recent work by Parente et al. (2011) successfully applied a blind source separation algorithm to extract end-members of hydrated minerals in CRISM data of the Martian surface. This method uses a non-linear transform to project each element of the cube into a new representation where the spectral sources (hydrated and mafic minerals here) of the observation appear geometrically separated in clusters and can be blindly isolated. The mineralogy of an observation as determined through a thorough manual investigation was successfully extracted by this method. Conversely, Gilmore et al. (2011) used superpixel segmentation on CRISM data as a means to both tackle noise effects and reduce the dimensionality of the data, and coupled it to the SMACC (sequential maximum angle convex cone) unsupervised spectral end-member extraction algorithm. Similar results were obtained with this method. To be noted however is that such approaches can be time-consuming and that the mineral identification of the putative detections by comparison with laboratory spectra is still required.

Here, we develop an end-member extraction algorithm directly coupled to the standard spectral parameter supervised classification method. With the addition of new noise-reduction processing steps, our goals are to provide a simple, robust and very fast way to screen large numbers of spectra for minerals and to attempt automatic identifications. The method developed here

can be viewed as an add-on to the standard processing methods used when dealing with imaging spectroscopy of planetary surfaces, and provides reduced-dimensionality maps and spectra representative of the mineral diversity in any observation. The strength of this approach lies in its very small processing time and robustness as it is an extension of well-proven techniques.

## 1.2. Hydrated minerals on Mars

The recent discovery of hydrated silicates on Mars (Poulet et al., 2005) has spawned a new and exciting era of exploration of the aqueous environments on early Mars. First detected from orbit by the OMEGA/Mars Express then CRISM/Mars Reconnaissance Orbiter instruments (e.g. Bibring et al., 2006; Mustard et al., 2008; Murchie et al., 2009) and now on the verge of being characterized in situ by the upcoming Mars Science Laboratory mission (Golombek et al., 2012), hydrated silicates, sulphates, and carbonates place strong constraints on the ancient surface/sub-surface, liquid water-bearing environments of Mars, and as such are of great exobiological importance (Poulet et al., 2009). Six years after their first discovery, more than a dozen different hydrated mineral species have been found (e.g. Ehlmann et al., 2011; Carter et al., in press), including phyllosilicates, zeolites, micas, hydrated (opaline) silica, hydrated and hydroxylated sulphates and carbonates. Hydrated mineral exposures on Mars number in the thousands (Mustard et al., 2008; Carter et al., 2011; Murchie et al., 2009; Poulet et al., 2007) and are mostly found in Noachian-aged impact structures, crustal and sedimentary units. Although the typical size of the hydrated mineral exposures is a few hundreds to thousands of CRISM pixels (a few sq kms) within the observations' field of view, a number of exposures are found with spatial extents down to a few pixels ( $\sim 0.002 \text{ km}^2$ ). Hence spatial resolution remains a limitation even from the Martian orbit. The dominant hydrated phases have undoubtedly been identified on Mars, but minor species occur and some may not have been identified yet, either because their extent is too small and/or because their spectral features are too subtle to be identified unambiguously. Although small in surface abundance, these minerals are nonetheless additional geochemical constraints on the aqueous environments of early Mars and should not be neglected. Their definitive identification require intensive processing of the observations so as to be extracted with sufficient signal-to-noise ratio from the spectrally unremarkable background lithology, composed primarily of iron-bearing dust and anhydrous mafic silicates. Better assessing the spatial extent of more common species is also important to understand on what scale they formed. As an illustration of the new algorithms, we present results of processing the CRISM dataset both to search for new phases and to extend knowledge of the distribution of previously discovered phases. Section 2 presents algorithms that address instrument noise and artefacts, and produce more accurate mineral indicator maps. Section 3 presents an end-member extraction algorithm which is based on the hydrated mineral indicator maps. Section 4 assesses the method efficiency on two studies of hydrated minerals on Mars. The issues raised and solutions proposed hereafter may be applicable to other imaging spectrometers as both the instrumental issues and observational biases are neither specific to CRISM nor to the Martian surface.

## 2. Processing the CRISM dataset

### 2.1. Surface reflectance

For the purpose of this work, we focus mainly on high-resolution targeted observations from the CRISM instrument

(18–36 m/pixel). CRISM measures reflectance spectra of the surface in the visible to near-infrared ([0.4–3.9] μm) spectrally sampled at ~6.55 nm (Murchie et al., 2007). We process the 'I/F' data available on the Planetary Data System (PDS) node which is calibrated radiance ( $\text{W m}^{-2} \text{ st}^{-1} \mu\text{m}^{-1}$ ) divided by a solar radiance spectrum whose intensity is scaled inversely by the square of the Mars–Sun distance. I/F data are then converted to surface reflectance through a two-step process accounting for photometric effects and atmospheric gas absorptions.

We assume that the Martian surface scatters light in a Lambertian fashion, i.e., that the reflected solar flux is isotropic and depends only on the surface reflectance  $r_\lambda$  and incident angle  $i$  (w.r.t. the local normal), and not on the emergence  $e$  or phase  $\phi$  angles. Photometric studies of the Martian surface (e.g. Johnson et al., 2006) have demonstrated that this hypothesis is true within 10% for phase angles between 25° and 100°, as is the case for most targeted CRISM observations. As this effect is largely independent of the wavelength, errors in absolute reflectance will not affect the mineral detection algorithms.

The CO<sub>2</sub>-dominated Martian atmosphere induces strong absorptions in the 1.4–2.8 μm range, some near saturation or saturated at CRISM's spectral resolution. These bands overlap the spectral signatures of hydrated minerals in the 1.4 and 1.9 μm regions and need to be removed. The atmospheric gas absorptions are corrected empirically using atmospheric transmittance spectra of Mars generated by rationing reflectance spectra at the base and summit of Olympus Mons, as detailed in Erard and Calvin (1997). The absorptions in the transmittance spectrum are automatically scaled to those in the surface reflectance spectra and removed. We use the improved method described in McGuire et al. (2009) that reduces post-correction artefacts in the 1.9 μm region by a better choice of the reference wavelengths upon which the spectra are scaled. This simple and robust method benefits from a very small computational time compared to radiative transfer-based corrections and is the most appropriate for processing large datasets.

Aerosols in the Martian atmosphere are known to induce a negative slope and artificially increase the absolute reflectance in the [1–2.6] μm range (Vincendon et al., 2009). Vincendon (2008) derived a method to correct reflectance spectra for the effect of aerosols. This latter correction is however too demanding in computational time to be implemented here. We will see that the correction method described in Section 2.3 allows one to tackle the photometric effects.

## 2.2. Spectral parameters

### 2.2.1. Description

Signatures of hydrated minerals are detected in CRISM data mostly within the 1.2–2.6 μm range, so the visible and mid-infrared (>2.8 μm) channels are not considered here. Hydrated minerals are detected through absorptions due to combinations and overtones of vibration bands of OH, H<sub>2</sub>O and X-OH, where X is typically Fe, Al, Mg or Si (e.g. Bishop et al., 2008). The most common bands are located near 1.4, 1.9 and 2.2–2.35 μm.

The spectral parameters test the presence of these diagnostic absorption bands as well as other features (slope or spectral shoulder) based on simple arithmetic between spectral channels. We use the definition introduced by Clark and Roush (1984):

$$SC = 1 - \frac{\langle r \rangle_{\lambda_{band}}}{\langle r \rangle_{\lambda_{continuum}}}$$

where  $r$  is the reflectance and  $\lambda_{band}$  and  $\lambda_{continuum}$  are each a small interval of spectral channels within which we compute the median value  $\langle r \rangle$  of the reflectance spectrum. Table 1 gives the list of spectral parameters used in our study which are tuned to the spectral features observed in hydrated minerals found to-date on Mars. This simple method contrasts with other approaches using blind source separation. It is asserted in the literature that one drawback of the spectral parameters used here is that they can only detect minerals for which the presence of diagnostic bands is tested. In principle, more complex methods should be

**Table 1**

Spectral parameters utilized for the detection of hydrated minerals on Mars. One-sided parameters (spectral slopes or shoulders) use one spectral interval in the continuum while two-sided parameters (measuring absorption depths) use 2, one on each side of the band. The superscript number indicates the number of spectra within each interval and over which the median value of the spectrum is calculated. 'D': Drop, 'BD': Band.

Target minerals	$\lambda_{band}$	$\lambda_{continuum}$	Ancillary detections
BD1.90			
Most hydrated minerals	[1.91–1.94] <sup>6</sup>	[1.73–1.85] <sup>19</sup> , [2.10–2.16] <sup>10</sup>	Water ice, atmospheric haze, low-Ca pyroxene
BD2.10			
Monohydrated sulphates	[2.06–2.16] <sup>16</sup>	[1.85–1.95] <sup>16</sup> , [2.20–2.24] <sup>7</sup>	Pyroxene
BD2.17			
Kaolins	[2.16–2.19] <sup>6</sup>	[2.05–2.15] <sup>16</sup> , [2.23–2.28] <sup>8</sup>	Pyroxene
BD2.20			
Al-smectite, hydrated silica	[2.20–2.25] <sup>8</sup>	[2.13–2.17] <sup>7</sup> , [2.25–2.29] <sup>7</sup>	Pyroxene
BD2.25			
Hydrated silica, jarosite	[2.20–2.30] <sup>16</sup>	[2.05–2.15] <sup>16</sup> , [2.35–2.40] <sup>8</sup>	Pyroxene
BD2.30			
Fe-smectite, Mg-carbonate	[2.28–2.31] <sup>6</sup>	[2.17–2.24] <sup>11</sup> , [2.35–2.38] <sup>6</sup>	High-Ca Pyroxene
D2.32			
Mg-smectite, chlorite, prehnite	[2.30–2.35] <sup>8</sup>	[2.10–2.20] <sup>16</sup>	
BD2.33			
Epidote, Fe/Ca carbonate	[2.32–2.37] <sup>8</sup>	[2.24–2.28] <sup>7</sup> , [2.39–2.43] <sup>7</sup>	High-Ca Pyroxene
BD2.35			
Prehnite, chlorite, epidote	[2.34–2.37] <sup>6</sup>	[2.26–2.31] <sup>8</sup> , [2.44–2.48] <sup>7</sup>	High-Ca Pyroxene
D2.45			
Zeolites, sulphates	[2.43–2.50] <sup>11</sup>	[2.28–2.35] <sup>11</sup>	
BD2.50			
Carbonates, serpentines	[2.47–2.53] <sup>10</sup>	[2.37–2.42] <sup>8</sup> , [2.58–2.63] <sup>8</sup>	
D2.6			
hydrated/hydroxylated minerals	[2.50–2.60] <sup>16</sup>	[2.10–2.20] <sup>16</sup>	Uncorrected water vapor
ICE			
H <sub>2</sub> O ice	[1.49–1.52] <sup>6</sup>	[1.29–1.31] <sup>4</sup> , [1.79–1.81] <sup>4</sup>	Monohydrated sulphates

more efficient in detecting new mineral phases. Gilmore et al. (2011) succeeded in extracting the mineralogy of CRISM observations which had not been manually investigated before, i.e. without a prior knowledge of its mineralogy. However, the final identification always resorts to a comparison with Earth laboratory spectra. Since there is a finite number of hydrous minerals that are documented on Earth and for which we have a spectrum, all the possible absorption bands can be tested with the spectral parameters. This method should therefore not be penalized. We consider that the foremost advantage of the spectral parameters lies in its reduced computational time, making this technique well suited to explore large datasets.

### 2.2.2. Issues with mineral mapping and overview of the proposed solutions

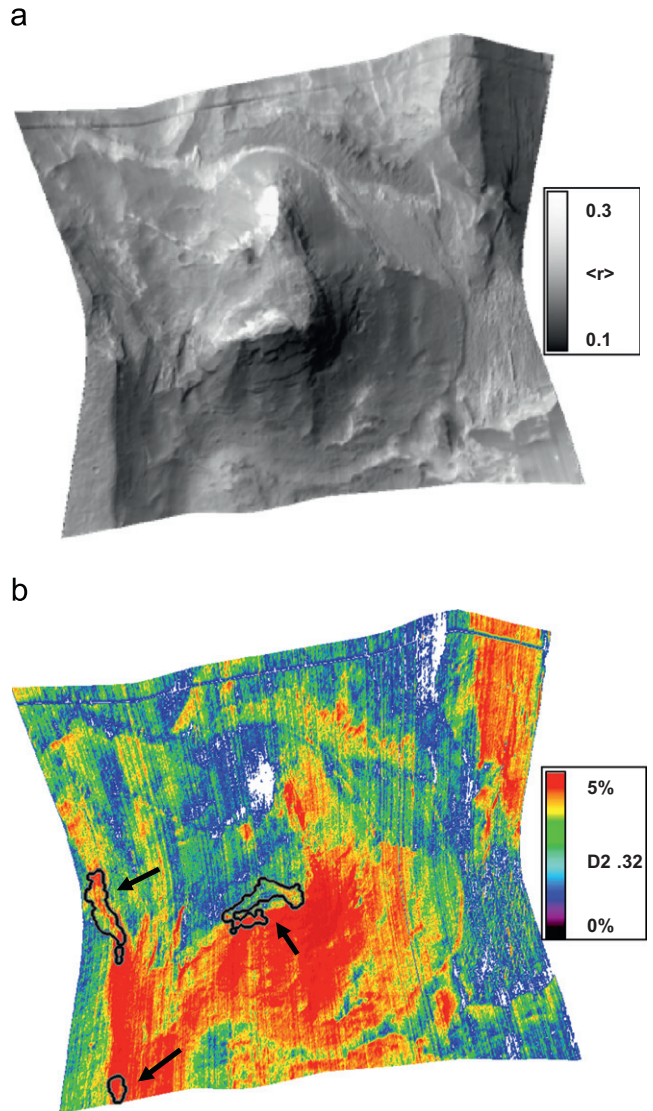
Although adequate for the processing of large datasets, these parameters and the corresponding hydrated mineral spectra are affected by both random and systematic errors: stochastic noise, the presence of instrument artefacts, variable observational conditions (photometric effects and aerosols), mixtures with mafic silicates or ices, and mixture with spectrally relatively neutral or featureless components such as dust. All of these factors can cause underestimation of the signatures of hydrated minerals, mask them altogether, or induce false positives.

Fig. 1 illustrates the effects caused by photometric geometry. The one-sided D2.32 parameter does not map actual hydrated mineral signatures (outlined in black after manual verification), but instead yields false positives wherever the spectral continuum is negatively sloped within shaded areas. These photometric effects are corrected as described in Section 2.3 by fitting and then removing a linear continuum to each spectrum.

We also investigated the effect of mixtures of hydrous silica with mafic minerals (olivines and pyroxenes), water ice and dust. We performed linear mixtures of hydrous silica with bands at 1.9, 2.2 and 2.3  $\mu\text{m}$  and found that the spectral parameter values for each of them was affected by the mixtures. Depending on the non-hydrous silica phase present, the absorption band depth was either over or under-estimated, leading to false positives and false negatives. No spectral parameter proved to be oblivious to all of the contaminants.

Quantitative abundance estimates of hydrated minerals on Mars (Poulet et al., 2008) have shown that even in areas with the strongest signatures, abundances of hydrated minerals are typically  $< 50 \text{ vol\%}$ , and that sites exhibiting the more common, weaker signatures for alteration have signatures suggestive of abundances  $< 20 \text{ vol\%}$ . This work illustrates that, overall, hydrated minerals are a minor component of Martian soils. A study of over 1200 CRISM observations displaying hydrated minerals reveals that the typical extent of the exposures is 2–4  $\text{km}^2$  (while some are detected down to a few pixels), whereas the typical CRISM image footprint is  $\sim 80 \text{ km}^2$  (Carter et al., in press). Signatures are also well correlated to local morphological features and seldom appear diffuse, whereas mafic mineral signatures and dust are found to be more homogeneously distributed. From these observations, we can subtract the non-hydrated ('neutral') mineralogy in each cube so as to highlight the localized hydrated sources. The method is described in Section 2.3.

Instrument artefacts that affect mineral identifications include spikes or bursts in the spectral domain and along-track (vertical in the image cube) striping in the spatial domain. Spectral spikes are corrected as described in Section 2.2.4, and occasional spurious pixels are identified and corrected as described in Section 2.2.5. The striping artefact is the most problematic one and is due to the push-broom technology of CRISM, in which



**Fig. 1.** Effects in spectral parameter maps induced by photometric geometry, for observation #FRT00009A8D displaying Fe/Mg phyllosilicates. (a) Mean NIR reflectance map showing shadows. (b) D2.32 map of Fe/Mg phyllosilicates: the strong signatures are all due to shadows while the manually verified signatures outlined in black and indicated by the black arrows do not stand out.

small detector element dependent calibration errors recurring in successive image lines appear as systematic stripes in the spatial domain of the image cube. The striping varies by image column, and is different for each wavelength and observation. A correction is proposed in Section 2.2.6. Small uncorrected optical distortions create another artefact known as spectral smile (or frown): the spectral bandpass of a single row on the detector has a central wavelength which shifts in the across-track direction, up to  $\sim 10 \text{ nm}$  or 1.3 speclets. Calibration files modelling the bandpass of each speclet quantify this effect. Although no correction of the smile is implemented, a common workaround is used as described in Section 3.2 to reduce the broadening of the spectral features.

Mineral identification is also affected by noise resulting from photon counting. This results from the very small detector instantaneous field of view ( $i\text{FOV} \sim 62 \mu\text{rad}$ ), the integration time that is limited by the along-track motion of the spacecraft, and in the IR a higher than anticipated background noise level due to operating the detector up to 15 K warmer than originally planned (Murchie et al., 2007; Seelos et al., 2011). As described

in Section 3.1, a very specific spectral stacking method is implemented to increase the SNR.

### 2.2.3. TRR2 vs TRR3

A new version of the radiometric calibration (TRR3) has been implemented and the CRISM dataset has been redelivered in that form in 2011. Improved instrumental calibration has also led to a more accurate continuum in the 1–2 μm region and to decreased artefacts at ~1.65 μm and ~3.18 μm. The TRR3 images are also characterized by reductions in both stochastic noise and instrument artefacts (Seelos et al., 2009, 2011). A three-dimensional iterative-recursive kernel filter is applied to reduce both systematic artefacts and stochastic noise. Although the latter step results in extremely minor loss of information, the processed I/F data benefits from improved S/N and reduced artefacts.

The corrections described hereafter were derived for the earlier, TRR2 version of the data. Although the reduced artefacts and noise may seem to render some steps described in this paper redundant, they are still valuable for the following reasons:

1. The kernel filtering in TRR3 data induces a slight spatial blurring of the reflectance and mineral maps. The filtered cube is also cropped on its edges resulting in a slightly smaller FOV than in TRR2 data.
2. While the filtered I/F data shows little to no striping, this is re-introduced after the atmospheric correction has been applied (see Fig. 2a). This striping results both from residual noise in the observations used to derive the atmospheric correction, and from sampling of small variations in the CO<sub>2</sub> band positions induced by the smile effect.
3. Residual artefacts are present in TRR3 data, especially at the warmer IR detector temperatures at which background noise was greatest.

The following processing steps can be applied similar to TRR2 or TRR3 image data after the photometric and atmospheric gas corrections.

### 2.2.4. Spike correction

Spikes in the CRISM spectra are corrected using a simple and rapid filter based on two criteria:

1. High variations in the spectra. We apply a 10-spectel large boxcar apodization function to each spectrum. For each spectel, if the relative variation between the raw and apodized spectra is above a threshold T%, then a potential spike is flagged.
2. For each potential spike flagged, the presence of an inflection point is tested based on a 3-spectel derivative of the spectrum. A spike is detected if both an inflection point and a relative variation > T(%) is found.

The spikes found are then corrected using nearest-neighbour interpolation.

To improve the removal of spikes in close proximity or in bursts, the algorithm is applied iteratively with a decreasing threshold from 4% to 2% in two iterations. Straightforward improvements to this method exist, but at the expense of increased computational time.

### 2.2.5. Spurious pixel and spectel correction

Spurious pixels are corrected both in the spatial and spectral domains. First, a small region of the cube is extracted from the centre of the field of view with a size of 15 × 15 pixels. For each spectel, if over 50% of the pixels within this sub-region have

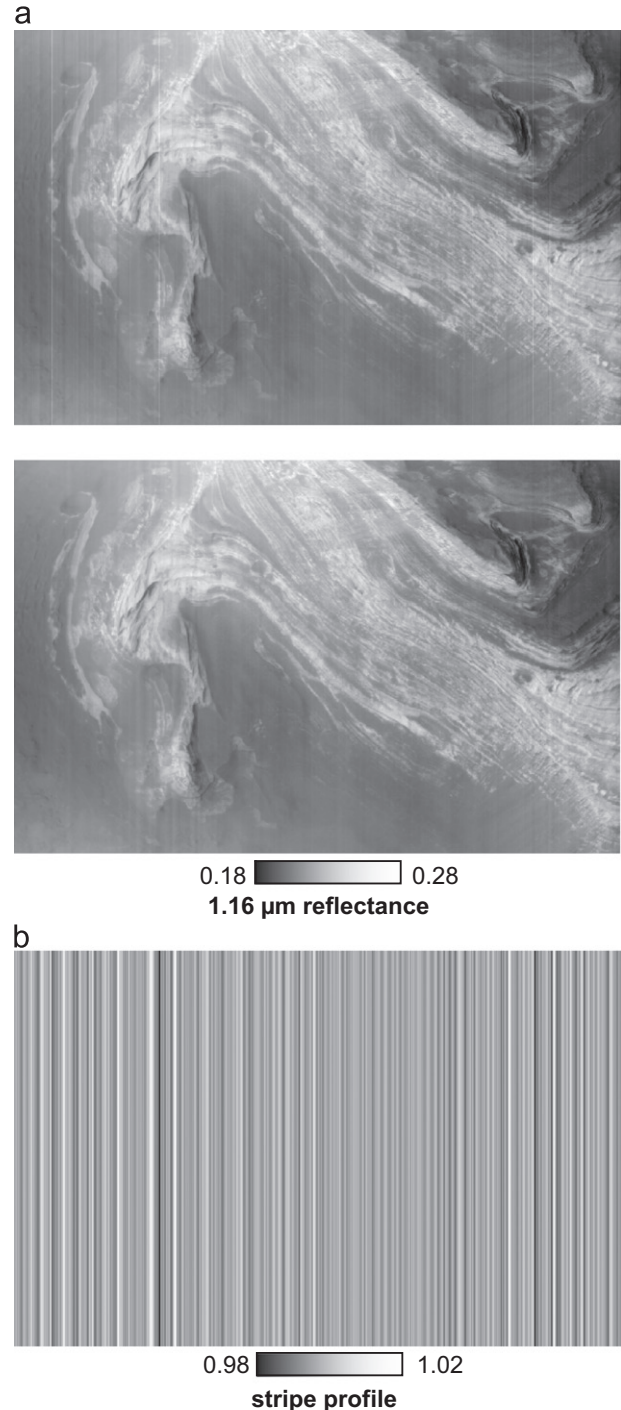


**Fig. 2.** De-striping of CRISM observation #FRT0000622B. (a) Raw (top) and de-striped (bottom) cube showing I/F at 1.16 μm. (b) Spike profile.

spurious values (with a reflectance near zero or above unity), then the spectel is flagged as spurious cube-wide and reconstructed through linear interpolation. Selecting a small portion of the cube to perform this test reduces the computational time.

Second, for each image at a given wavelength, we apply a 2D apodization filtering using a 15-pixel 2D boxcar kernel. Any pixel with a relative variation > 30% between the image and the apodized image is flagged as spurious and replaced by its apodized value. This threshold is based on the relative variation of the reflectance instead of the more accurate variation from the standard deviation so as to minimize processing time. We did not

find this choice to significantly degrade the filter. The conservative threshold of 30% allows the removal of a number of spurious pixels while not removing an appreciable amount of information. We benchmarked this value by looking in particular at thin layers of light-toned sediments within the Holden delta of Mars which are amongst the smallest features observable at the CRISM resolution and are highly contrasted. While spurious pixels are removed, the light-toned strata remain intact and no blurring occurs.

### 2.2.6. Striping correction

Accurately correcting the striping pattern (which is unique to each observation and each wavelength) is non-trivial, owing to difficulties in distinguishing the stripe profile from spatial variations of the reflectance. We model the stripes as a multiplicative noise to the data which to the first order is constant in the along-track direction. Residual, partial stripes are also present however, and will be tackled in Section 2.3.1. For each wavelength, we calculate the mean reflectance in the along-track direction thus building a one-dimensional profile of column-averaged reflectance. This profile has low frequency variations due to the across-track spatial variations of the reflectance in the field of view, and we hypothesize that high spatial frequency (small scale) variations in the reflectance are removed by the along-track averaging. The remaining high-frequency ‘noise’ in the profile is therefore the stripe profile. It is extracted by applying a two-step filter to the column-averaged reflectance profile: spike removal followed by a 3-pixel Lorentzian kernel apodization. The spike removal algorithm is the same which was applied on the spectral data in Section 2.2.4 and is used to remove major ‘spikes’ which would affect the apodization. The sharp Lorentzian kernel allows better filtering of the high-frequency stripe energy than a boxcar window. We then extract the 1-D stripe profile by dividing the initial profile by the filtered profile. Finally, within each column, we divide every pixel by the corresponding column value of the spike profile. The algorithm is automatically applied in each band of the cube (at each wavelength). An example is provided in Fig. 2.

An issue will arise if an observation displays a structure with a high contrast in reflectance in the along-track direction while being very narrow in the across-track direction. While column-to-column striping is removed, longer wavelength striping (the size of the structure across-track) will appear. This issue is largely solved if, while building the across-track profile, a switch is made from a blunt entire-column averaging to a 3-segment average or median, each segment being one-third of the total along-track length. This additional averaging step reduces the effect of such structures if their extent is not close to the entire length of the field.

## 2.3. Deriving mineral maps

### 2.3.1. Method

Nine steps are implemented to derive spectral parameter maps based on a reflectance cube processed for instrument artefacts as described in the previous section:

1. Each spectrum is fitted then divided with a linear continuum using spectels at  $\sim 1.75$  and  $\sim 2.14 \mu\text{m}$  where few hydrated minerals absorb. This step is used to limit the effect of high dust or aerosol opacity, shadows, and photometric effects. Although this spectral continuum correction does not improve the detectability of the hydrated signatures, it does yield a more homogeneous, continuum-removed cube more suitable for step #3.
2. Residual striping in the spatial domain is removed by running the algorithm described in Section 2.2.6 but with a larger

Lorentzian window (typically 60 pixels instead of 3). This removes large-scale (10s of pixels) across-track variations in the mean reflectance as can be seen in the centre of the observation of Fig. 2.

3. The neutral mineralogy is subtracted. We assume that each spectrum of the surface to be a linear mixture of neutral minerals and at times of hydrated minerals. Based on the assumption that the neutral mineralogy is uniform on a spatial scale that is larger than the hydrated mineral exposures, we can subtract a spatially averaged contribution of these neutral minerals to each spectrum of the observation. Once subtracted by this average neutral spectrum, pixels showing only neutral minerals will have a near-to-null residual spectrum. On the other hand, pixels originally displaying mixtures of hydrated minerals and neutral minerals will have their neutral component removed so that only the hydrous signatures will remain, thus highlighting them. The subtraction is done on a column-per-column basis so as to minimize the effect of spectral smile and residual stripes: we subtract to each spectrum of a given column the average spectrum over that same column. Similar to the de-striping algorithm, this step is improved by taking for each column the median spectrum of a 3-segment average instead of a simple average spectrum over the entire column.
4. Residual spurious pixels are removed as described in Section 2.2.5 with a cut-off threshold of 5%. This lower threshold is made possible by the linear continuum removal in step #1 which reduces the variance in reflectance.
5. The resulting relative reflectance cube is re-normalized using the same linear continuum adjustment as in step #1 to avoid negative values in absorption bands.
6. Retrieval of very faint hydrated signatures or signatures mixed by mafic minerals requires an additional continuum removal step. We remove a curved continuum either by using a low-pass Fourier filter or an adjustment of the spectra using tie-points. In the latter case, polynomial curve fitting is inadequate as it lacks robustness and requires a lot of computational time. We use a fast and robust method to remove the continuum based on tie-points. Each spectrum is down-sampled to 10 spectels selected outside hydrated mineral absorption bands. This low resolution spectrum is then re-interpolated to the original spectral resolution and appears as a chain of segments for which the points were chosen outside the hydrous absorption bands. The continuum is derived by applying a 40-pixel large boxcar apodization function to this segment chain. The resulting smooth continuum provides a good local adjustment around each absorption band while being much faster to compute than a polynomial curve adjustment or a Fourier filter. Although this step improves the detectability of absorption bands, it has the caveat to fit large features such as the  $2.4 \mu\text{m}$  drop in zeolites or the overall concave shape from  $2.1$  to  $2.6 \mu\text{m}$  indicative of the presence of hydrated minerals. As a result, these features are underestimated or even masked and hence this step is not applied to single-sided spectral parameters (see Table 1).
7. The set of spectral parameters described in Table 1 is calculated.
8. Residual errors are occasionally present in the spectral parameter maps and appear as vertical, small-scale and large-scale artefacts which vary in the across-track direction and are due to effects of the spectral smile, errors in step #3, or residuals from the de-striping algorithm when an observation is highly heterogeneous. These artefacts appear in the parameter maps as additive noise with an extended vertical dimension, they can therefore be removed from the maps using an algorithm similar to that of step #3. Each pixel of a given column is subtracted by the average value of the map over the entire column, thus ‘flattening’ the parameter maps.

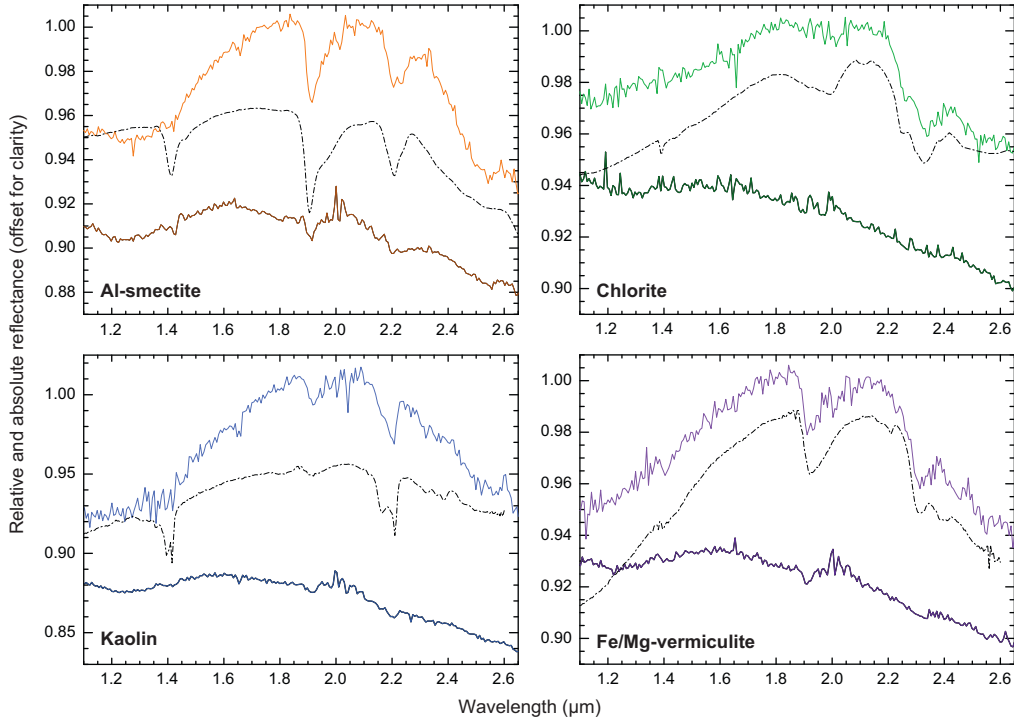


**Fig. 3.** Spectra of four different hydrous minerals from pre-processed and processed cubes (all from observation #FRT0000ADA4). The top, light-toned colour spectrum of each frame is the relative reflectance spectrum corrected for the instrument artefacts and with the neutral mineralogy subtracted. Each spectrum shows a different hydrous mineral detected in this observation. The two bottom spectra of each frame are the absolute reflectance spectra used to derive the top spectra. The dark-toned spectrum shows the pre-processed hydrous mineral signature and the light-toned spectrum is the corresponding column average used to subtract the neutral mineralogy. The dashed black lines are laboratory spectra providing good matches to each exposure. Each spectrum is a 9-pixel average. (For interpretation of the references to colour in this figure legend, the reader is referred to the web version of this article.)

9. The final post-processing step removes residual stochastic noise in the maps. The study of many CRISM observations has shown that hydrated minerals are dominantly clustered within the field of view. Isolated (un-clustered) pixels are therefore either random noise or detections of hydrous mineral exposures at the limit of the CRISM spatial resolution. We consider the majority of these un-clustered pixels to be noise and remove them from the maps. While a few single-pixel exposures are bound to be removed with this criterion, clustered detections have much stronger spectral signatures because they experience less sub-pixel mixing with neutral minerals. Removing a few small and isolated exposures therefore removes very little useful information, while removing a lot of random noise. We use a simple algorithm which detects for each pixel ( $x,y$ ) the number of its eight closest neighbours which are not equal to zero. If this number is above a certain threshold then this pixel is flagged as part of a cluster and kept, otherwise it is removed. The conservative value for the threshold used is 2. This step may be applied iteratively to reduce small clusters of spurious pixels. A standard two-pass is sufficient and keeps the loss of information to a minimum.

As shown in Fig. 3, weak signatures hardly distinguishable in the original spectra become clearly visible and the mineral phase is more easily identifiable. In the case of minerals with well identifiable bands (e.g. kaolinite), we extract spectra that match well the laboratory band shapes and positions. An advantage of this method is that it lessens or removes entirely the need to use spectral ratios to enhance mineral signatures.

Fig. 4 illustrates how photometric effects are addressed by these processing steps. For this observation we map the D2.32 one-sided spectral parameter calculated from (a) the cube processed only to I/F, (b) the cube processed only for instrument

artefacts, and (c) the cube processed using all of the above steps (but the tie-points-based continuum removal). Although striping is removed in Fig. 4b, shading still affects the map and the actual signatures only become clear in Fig. 4c. In this processing step we use a threshold of 0.5% instead of 0% to reduce residual noise.

Fig. 5 illustrates the improved detectability of hydrated mineral signatures in an observation with both high aerosol opacity ( $\tau > 2$ ) and localized mixtures with mafic silicates. Here we map the two-sided BD1.90 parameter using data (a) treated for instrument artefacts, (b) with all the above steps except the tie-points continuum removal, and (c) with the tie-points continuum removal added. The first map detects no hydrated signatures and there are false positives on the right edge (white arrows). CRISM being gimballed with a  $\pm 30^\circ$  along track variation in phase angle, aerosol contribution is highly variable within the field of view and step #1 becomes necessary. In frame (b), after subtracting the neutral mineralogy, most hydrated signatures become visible but a false positive still occurs (white arrow) because of a localized strong pyroxene signature. After the tie-points continuum removal in frame (c), the map has an improved sensibility and after a thorough manual verification, we find that false positives are removed entirely and no mineral exposure is left out.

### 2.3.2. Applications to CRISM multi-spectral observations

The same method has been applied successfully to multi-spectral CRISM (100–200 m/pixel, nadir pointed) observations. The very long along-track dimension precludes the use of an entire column average as the neutral mineral components are seldom homogeneous over several degrees of latitude. Instead, a sliding algorithm is derived over segments of few hundreds of pixels long and which can be adapted to each observation. Fig. 6

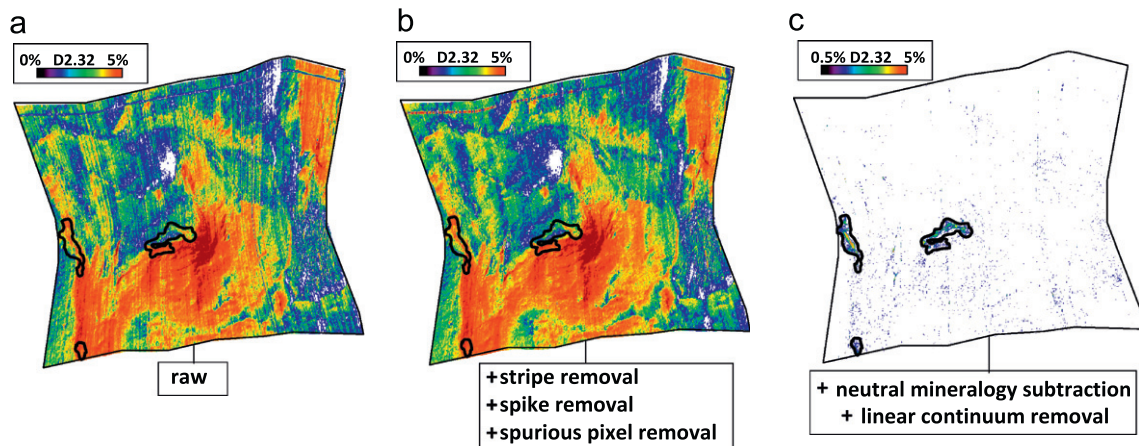


**Fig. 4.** Improvement of spectral parameter maps (1): example of observation #FRT00009A8D and parameter D2.32 mapping Fe/Mg phyllosilicates. (a) D2.32 map from the raw surface reflectance cube. (b) D2.32 map from the cube processed for instrument artefacts. (c) D2.32 map from the cube with neutral mineralogy subtracted and linear continuum removed. Similar to Fig. 1, the actual Fe/Mg phyllosilicate signatures are outlined in black.

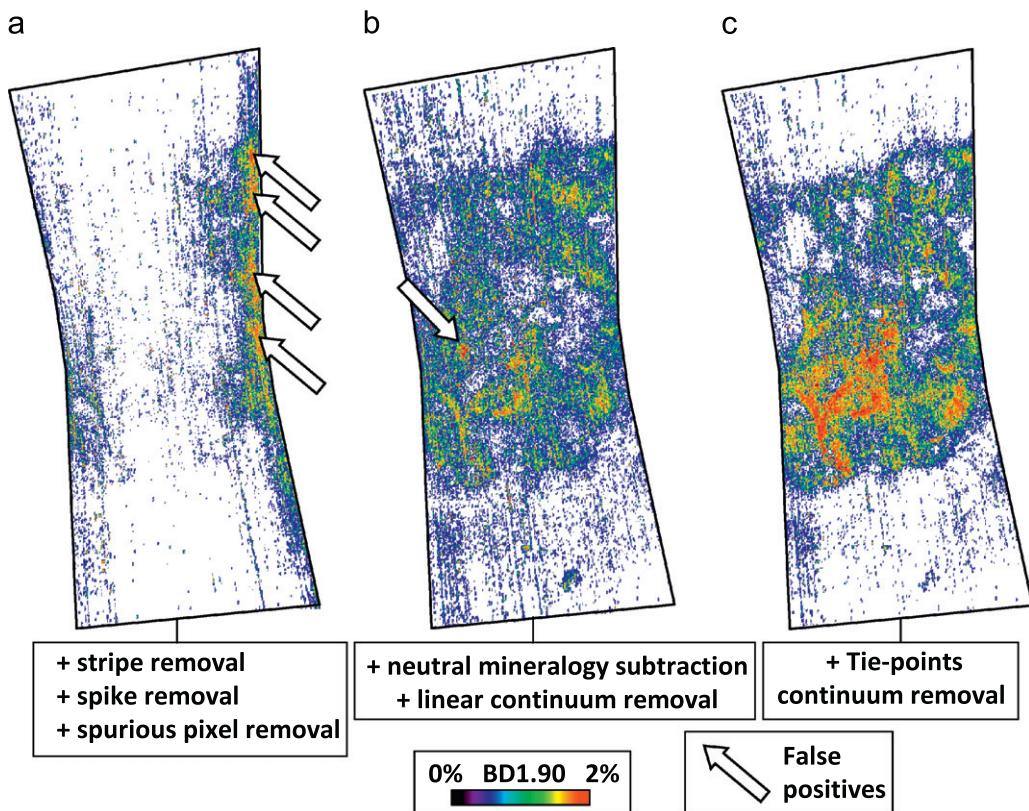


**Fig. 5.** Improvement of the spectral parameter maps (2): example of observation #HRL0000C75D and parameter BD1.90 mapping mixtures of chlorites and clays. (a) BD1.90 map from the surface reflectance cube processed solely for instrument artefacts. (b) BD1.90 map from the cube with neutral mineralogy subtracted and linear continuum removed. (c) BD1.90 map after additional tie-points continuum removal necessary due to the presence of strong pyroxenes signatures. False positives are indicated by the white arrows.

shows an example for a CRISM observation using the zeolite parameter D2.45. Here, the reference wavelengths used to derive the D.2.45 parameter are the same as for the targeted observations as described in Table 1 but averaged on fewer spectrals given the lower spectral binning of multispectral observations ( $\sim 54$  nm/channel). We used a sliding algorithm with a window size of 500 pixels in the along-track direction. The processed map (top right) has fewer false positives due to shading compared to the pre-processed map (top-left). The reference mineral map used for the comparison is provided by an overlapping targeted

observation using the same spectral parameter (bottom right) and verified by hand. The processed multi-spectral and targeted observations are in very good agreement.

### 2.3.3. Mineral discrimination using spectral parameters

Because some hydrated minerals have very similar spectral features, we cannot discriminate between them directly from individual spectral parameter maps (as those of Table 1). Identifications could be possible by a direct comparison with laboratory

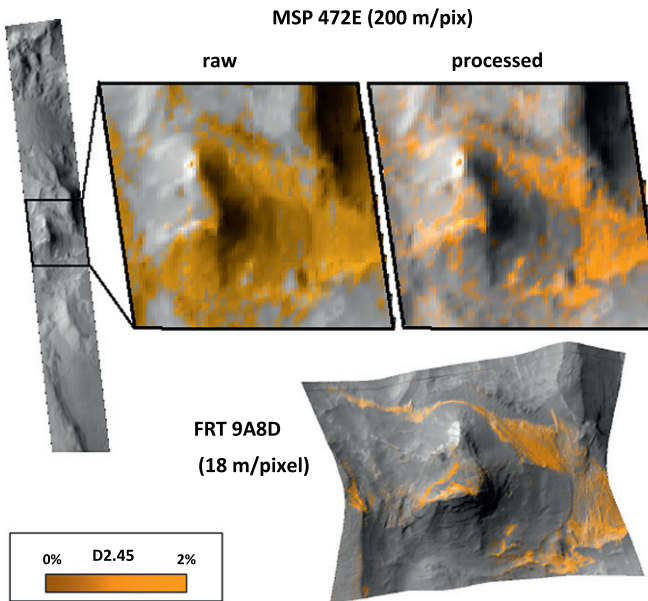


**Fig. 6.** Processing of a multi-spectral CRISM observation of zeolites (D2.45 parameter). The processed map (top right) has reduced false positives due to shading and an increased detection sensibility. Comparison is made with an accurate zeolite map from an overlapping high-resolution observation (bottom right) showing good agreement.

**Table 2**

Spectral parameter combinations for the automated identification of hydrated minerals. Each of the 11 new combination maps are a combination of required and rejected spectral parameter maps.

End-member	Criteria required	Criteria rejected
Zeolites, sulphates	BD1.9, D2.45	D2.32, BD2.30, BD2.20
Chlorites	D2.32	BD2.20, BD2.30, D2.45
Epidote	BD2.33	BD2.30
Al smectites/micas	BD2.20	BD2.17
Kaolins	BD2.17	BD2.20
Fe/Mg Clays	D2.32	D2.45
Fe smectites	BD2.30	–
Hydrated silica	BD2.25	BD2.17
Prehnite	BD2.35	–
Carbonates, serpentines	D2.32, BD2.50	–
Mono-hydrated sulphates	BD2.10	–

spectra as will be described in Section 3.3, but such a technique cannot be applied to every pixel of every observation because of the long computational time required. To better discriminate the mineralogy in a time-efficient way, we use combinations of spectral parameter maps based on those defined in Table 1. We discriminate specific mineral species by requiring for each pixel one to several parameters to yield a positive detection while requiring others to yield a negative detection. For example, zeolites or sulphates are detected only if both the parameters BD1.90 and D2.45 show positive detections while parameters D2.32, BD2.30 and BD2.20 do not (Table 2). In this case, the combination removes contaminations in the maps from several other hydrous minerals (opaline silica, Al/Fe/Mg smectites and chlorites). We also map an ice spectral parameter which is systematically masked out of all combinations of parameters maps. A total of 11 combined parameter maps encompassing the entire diversity found to-date on Mars are chosen (Table 2) and listed here according to the mineral(s) they detect: (i) Al smectites and micas, (ii) Fe smectites, (iii) Fe/Mg clays (smectites, vermiculites, micas), (iv) chlorites, (v) prehnite, (vi) kaolins (kaolinite, halloysite), (vii) zeolites and poly-hydrated sulphates,

(viii) mono-hydrated sulphates, (ix) hydrated (opalized) silica, (x) carbonates and serpentines and (xi) epidote.

At this point, the pipeline yields a cube with reduced instrument artefacts and optimized for the detection of hydrated minerals, as well as a set of 11 maps which are automatically generated for a rapid assessment of the observation's mineralogical relevance.

### 3. Automated end-member extraction and identification of mineral exposures

This section describes the tools developed to automatically extract and identify 'end-member' spectra of hydrated phases from CRISM observations. This end-member extraction procedure is an add-on to the processing steps presented thus far.

#### 3.1. Spectral stacking

The previous step provided 11 maps each corresponding to one to a few different minerals (hereafter called end-member maps). We extract the corresponding spectra for each end-member map. This is done by performing a spatial average (or stacking) over all the non-null pixels of the end-members maps. Stacking (Dole et al., 2006) increases the signal-to-noise of the resulting average spectra, thus allowing a better characterization of major absorption bands, but it also has the advantage of allowing very weak spectral features to be identified. These features may be otherwise lost in the noise level of single-pixel spectra and too narrow to be mapped directly using spectral parameters (typically bands less than 2–3 spectels wide). Since stacking allows identifying both the main and minor spectral features, it is a robust statistical tool against artefacts in the spectra that can resemble absorption bands: the more bands are detected in each spectrum, the less likely they are all due to artefacts. False identifications are thus reduced. The best test is the 1.35–1.55 μm Metal-OH vibration band which is present in all hydrated/hydroxylated minerals. On Mars, this band is always narrow and shallow, of the same order as the stochastic noise, and is seldom unambiguously detected in a single pixel nor can it be accurately mapped using a dedicated spectral parameter. By performing spectral stacking based on end-member maps that test the main absorption bands, this minor band becomes visible.

Another issue tackled by stacking is the contamination between spectral parameters. Contaminations by several minerals can be assessed by conducting a bootstrap analysis on the set of selected spectra to be stacked, as is exemplified in Fig. 7. Here we map hydrous minerals in observation #FRT0000622B based on the D2.32 and BD2.30 spectral parameters. While the BD2.30 parameter uniquely maps Fe-rich smectites here, the D2.32 parameter maps Fe-/Mg-rich clays but is also contaminated by the presence of zeolites (justifying the combinations shown in Table 2). Fig. 7a shows the parameter maps of BD2.30 (red), D2.32 (green). The intersection of both maps appears in orange and shows that the BD2.30 map is entirely contained within the D2.32 map, the latter being contaminated by zeolites. We perform a spectral stacking over the region of interest circled in white which encompasses regions where both maps overlap and regions where only the D2.32 map is non-zero. Results are shown in Fig. 7b and c. The error bars on the spectra are the result of the bootstrap analysis of the statistical sample: small errors indicate the distribution likely contains only one mineral specie, while large errors imply the end-members are contaminated by several minerals. By selecting only pixels with a non-zero value of the BD2.30 parameter, we see very small errors indicating that only one spectral end-member is present, a Fe-rich smectite. On the

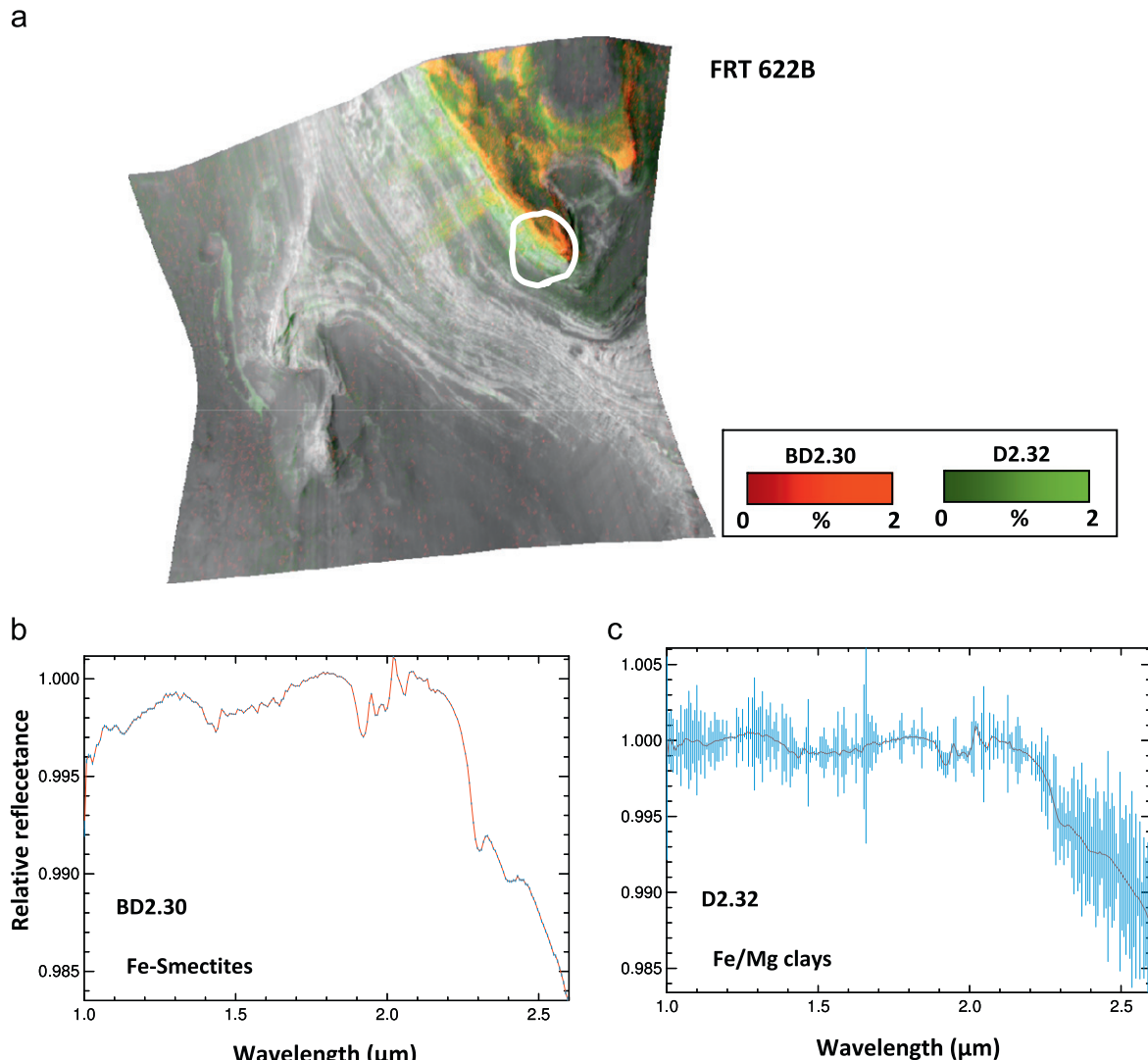


**Fig. 7.** Spectral stacking and bootstrap analysis to tackle mineral contaminations in spectral parameter maps. (a) Parameter maps of BD2.30 (red) and D2.32 (green) for observation #FRT0000622B, regions where both maps overlap are in orange. Circled in white is the region of interest over which spectral stacking is conducted. (b) Average spectrum from the spectral stacking based on the BD2.30 map. (c) Average spectrum from the spectral stacking based on the D2.32 map. The error on the distribution assessed using bootstrap analysis is shown in blue. The left spectrum is a pure Fe-smectite (small errors), the right spectrum is a mixture of Fe-smectite and zeolite (large errors). (For interpretation of the references to colour in this figure legend, the reader is referred to the web version of this article.)

other hand, by selecting all non-zero pixels from the D2.32 parameter, we see large error bars reflecting a large spectral variance within the sample. This indicates that this average spectrum is a mixture of zeolites and Fe-rich smectites. Application to all 11 end-member maps of Table 2 allowed us to verify contamination was minimal.

### 3.2. Spectral end-member extraction algorithm

The spectral stacking based on the end-members maps allows the extraction of spectral end-members. The following four steps are used to increase the strength of the signatures extracted:

1. We build a histogram of each end-member map, counting the number of pixels per map value. This step is used to set lower and upper bounds for the map values. A study of the histogram over 60 CRISM observations displaying hydrated minerals shows that the typical profile is a sharply decreasing pixel count as a function of absorption depth, with a maximum pixel count between 0% and 0.5% absorption depth. High map values contain the strongest mineral signatures, but their lower

frequency results in high-stochastic noise when stacking only on them. Residual artefacts in the data tend to yield false positives with high parameter values, so keeping only the higher values can also amplify these artefacts instead of the actual signatures. In this first step, we set a lower bound as the maximum of the histogram calculated for each observation (typically between 0% and 0.5%) in order to keep a statistical number of pixels. The upper bound is set by calculating the total Euclidean norm of the histogram and keeping all values falling within the first 99% of this norm. This removes a small number of very high values which usually are artefacts. It was determined empirically that using a norm-based cut-off instead of a simple absorption depth-based cut-off removes more artefacts.

2. The second step involves the weighting of the histogram values. We use a nine-order polynomial fit to each histogram. The weighting function is the inverse of the polynomial fit, thus placing higher weights on high (but less frequent) parameter values. This step allows increasing the signal-to-noise of the end-member spectrum while keeping the absorption features strong.

3. The third step improves further the stacked spectrum by weighting pixels using the clustering filter described in Section 2.3.1. Each map has already been filtered with this algorithm with a threshold value  $N_{\text{cluster}}^{\text{threshold}} = 2$ . All pixels remaining after this filter are given a weight equal to 1. The end-member maps are then additionally filtered with a higher value  $N_{\text{cluster}}^{\text{threshold}} = 4$  which only keeps highly clustered pixels. These clusters are considered less prone to artefacts and to mixtures with neutral components, and a higher weight is placed upon them. Their weight is expressed as  $N_{\text{cluster}}^{t=2}/N_{\text{cluster}}^{t=4} (> 1)$ , where  $N_{\text{cluster}}^t$  represents the total number of available pixels in the map after applying each filter. Finally, before stacking each individually weighted spectrum into the end-member spectrum, each of them is re-interpolated to the central wavelength to account for the smile effect.

The final algorithm is summarized below with WF the weight function and SP the end-member:

$$\begin{aligned} SP\lambda &= \frac{\sum_{lb < sc(x,y) < ub} r_\lambda(x,y) \cdot WF(sc(x,y))}{\sum_{lb < sc(x,y) < ub} WF(sc(x,y))} \\ WF(sc(x,y)) &= \frac{1 + \delta_{(x,y)}^{(x,y)\text{cluster} = 4} \cdot \left( \frac{N_{\text{cluster}}^{t=2}}{N_{\text{cluster}}^{t=4}} - 1 \right)}{\sum_{d=1,9} a_d \cdot sc(x,y)^d} \end{aligned}$$

- $r_\lambda(x,y)$  is the relative reflectance at pixel  $(x,y)$ .
- $sc(x,y)$  is the spectral parameter value at pixel  $(x,y)$ .
- $lb$  and  $ub$  are the lower and upper bounds as determined from the histogram of each spectral parameter.
- $\delta_{(x,y)}^{(x,y)\text{cluster} = 4}$  refers to all pixels remaining after the clustering filter with threshold = 4.
- $a_d$  are the coefficients of the nine-order polynomial fit of the histogram.

Fig. 8 illustrates for a kaolin mineral the usefulness of each processing step described in this section as a means to better extract the spectral end-member. The green spectrum is a blunt average over all pixels of the kaolin end-member map with an absorption depth lower threshold of 0%. Signatures are better extracted (with little loss of signal-to-noise) after each additional step (orange then brown then red).

### 3.3. Semi-automated identification

Each observation now has a reduced dimensionality of 11 end-member maps (Table 2) and corresponding spectra. Automated

identification of the spectra is attempted by least-square fitting of a sample of ~100 laboratory spectral from the RELAB and USGS spectral repositories. Each end-member spectrum is fitted with a combination of laboratory spectra and a second-order polynomial. Weighting is applied and is adapted to each end-member's absorption bands. The polynomial function allows one to account for photometric effects, the presence of dust, aerosols and iron-bearing absorbents that can modify the spectral shape. The goodness of the fits are assessed by calculating the RMS error and only the three laboratory spectra with the lowest error are selected and plotted alongside the end-member. A graphical output of the end-members with the best library adjustments and mineral maps is generated for rapid browsing of each observation.

## 4. Evaluation of the methodology

In this section we propose an evaluation of the technique and summarize its main advantages and drawbacks.

### 4.1. Accuracy of the spectral end-member extraction

We assess the accuracy of the end-member extraction algorithm by studying a large sample of 502 observations in the northern Hellas Province. The study area extends from the southern margin of Hellas to Tyrrhena Terra, bordered by Terra Sabaea to the West and Hesperia Planum to the East ([50;105]°E, [−35;−5]°N). Each observation is inspected manually after having been processed by our data reduction pipeline that reduces instrument artefacts and subtracts the neutral mineralogy. This careful inspection of the mineralogy defines our reference sample, which was then screened using the automatic end-member extraction analysis.

Out of the 502 observations, the manual inspection led to positive detections of hydrous minerals in 360 observations. While in about 50% of the cases only one hydrated phase is present, up to 6 can be found in single observations. We compare these results to the end-member extraction method. We use one simple spectral parameter map and four spectral end-member maps: the BD1.90 parameter common to most hydrated minerals but which does not allow their discrimination, and the end-members of chlorite, prehnite, Fe/Mg clays and zeolites/sulphates as defined in Table 2. The other hydrous minerals are too rare in this region to be statistically significant. The resulting five end-member spectra extracted for each observation are inspected visually. Using the BD1.90 parameter, 335 out of 360 sites are detected with the end-member extraction, yielding an accuracy of ~93% (Fig. 9). Inspection of those that were not detected shows that the extraction failed not because of a lack of sensibility of the algorithm but because the spectra extracted were either not physical, dominated by water ice or dominated by artefacts in the 2 μm atmospheric bands. In addition, no false positive is identified by the extraction technique. These results make us confident on the reliability of our automatic detection method.

While the broad parameter yields high accuracy for detecting hydrated minerals, it cannot identify the mineral family. To do so, we compared results with the four end-members, and the accuracy drops to about 60% on average. The Fe/Mg clays end-member accuracy is difficult to estimate precisely: this mineral class encompassed smectites, possible micas but mostly vermiculites and/or inter-stratified minerals which are often hard to discriminate from chlorite-rich minerals (pure chlorite and corrensite). Some mis-identifications between the two classes are expected with the end-member extraction. We however emphasize that even with a manual investigation it is also tricky to

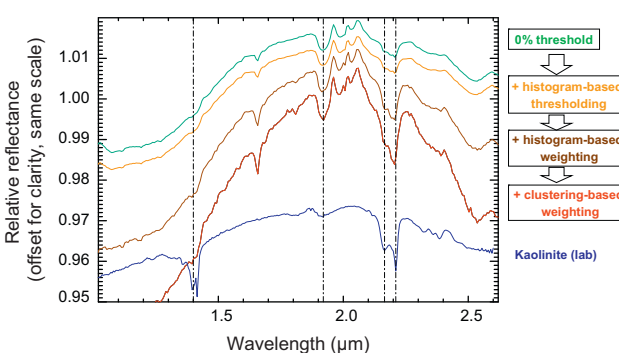


Fig. 8. End-member extraction of kaolinite in observation #FRT0000ADA4. The spectral contrast is improved without significant increase in the noise level with each added step. (For interpretation of the references to colour in this figure legend, the reader is referred to the web version of this article.)

discriminate between these phases. Prehnite is also very difficult to identify because it is nearly always mixed with chlorite and the latter clearly dominate the spectrum. A careful manual investigation was required to identify prehnite. These results show that the method can provide a rough (but still very useful and fast) identification of the mineralogy within an observation.

#### 4.2. Example of application: identification of epidote

##### 4.2.1. Epidote

By using the data reduction and extraction method presented in this paper, we report the first detection on Mars of the Fe-bearing hydroxylated sorosilicate epidote ( $\text{Ca}_2(\text{Fe},\text{Al})\text{Al}_2(\text{SiO}_4)_3(\text{Si}_2\text{O}_7)\text{O}(\text{OH})$ ). Epidote is a mineral found typically in hydrothermal, contact metasomatic and low-grade metamorphic environments. It has also been found on Earth in impact melts (Lounejeva et al., 2003). Typical formation temperatures are greater than all

other hydrated minerals found on Mars to-date ( $> 250^\circ\text{C}$ ). On Earth, it is found in higher-grade metamorphic facieses than zeolites and prehnite.

Epidote features three minor OH vibration band overtones at 1.357, 1.409 and 1.548  $\mu\text{m}$  (Clark et al., 1990), the latter being the deepest in all available laboratory spectra. Two major bands, an order of magnitude greater than at 1.55  $\mu\text{m}$  occur at 2.254 and 2.339  $\mu\text{m}$  as combinations of OH and Fe–OH vibration bands. Although not documented in laboratory studies, additional minor bands are present in all library samples at 1.69, 1.83 and 1.95  $\mu\text{m}$ . While the sharp shape and close proximity of the two major bands is unique to epidote, mixtures with other minerals and high noise levels preclude an identification based solely on them. Chlorite and prehnite in particular could yield rather similar bands in the region.

##### 4.2.2. Detections

Epidote was first tentatively detected on the floor of a  $\sim 18$  km large crater impacting the volcanic plains of Hesperia Planum (observation #FRT00008FBB;  $106.8^\circ\text{E}$ ,  $-11.7^\circ\text{N}$ ). Given the subtle spectral features of epidote in the  $1.3$ – $1.95$   $\mu\text{m}$  range, its detection was made possible by the processing steps introduced here. Following this first detection, we derived the BD2.33 spectra parameter (see Tables 1 and 2) and performed end-member extraction on a sample of over 2000 CRISM observations.

Epidote end-members are compared to a laboratory spectrum and sorted by RMS error, and the first five with lowest error were selected after visual inspection. The CRISM spectrum shown in Fig. 10 is the average end-member spectrum from these five observations. The major 2.25 and 2.34  $\mu\text{m}$  bands are detected alongside the minor band at 1.55  $\mu\text{m}$  (depth is  $3.6\sigma$ , above noise level). Close examination also yields additional bands at 1.69, 1.83 and 1.95  $\mu\text{m}$  with depths slightly above the noise level and consistent with those found in laboratory spectra of epidote. This illustrates how spectral stacking based on a major absorption band can yield other minor bands otherwise un-observed in individual spectrum, and allowing the definite identification of the mineral.

All five epidote outcrops detected so far on Mars are very small ( $< 1 \text{ km}^2$ ). One detection in Nili Fossae occurs less than 1 km away from the present extent of Syrtis Major lava flows, at proximity to olivine altered into lizardite (Fig. 11) for which a hydrothermal origin was put forward (Ehlmann et al., 2009). Three other detections are connected to an impact structure near or over a volcanic unit (observations #FRT00005D41,

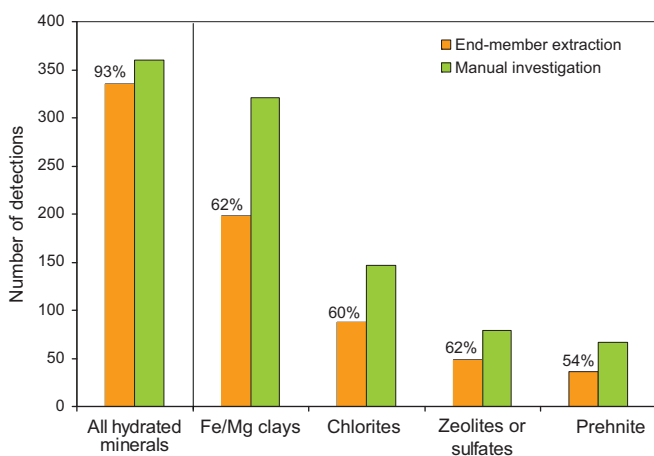


**Fig. 9.** Assessing the accuracy of the end-member extraction method by comparing mineral identifications to a manual investigation for a sample of 502 observations in the northern Hellas province. The two bars on the left show the number of hydrous mineral detections at the outcome of the manual investigation (green) and by running the end-member extraction on the BD1.90 spectral parameter (orange). Although the accuracy is high, the BD1.90 parameter cannot distinguish the mineral classes. Accuracy is lower ( $\sim 60\%$ ) for specific mineral classes, here: Fe/Mg clays, chlorites, zeolites/sulphates and prehnite. (For interpretation of the references to colour in this figure legend, the reader is referred to the web version of this article.)

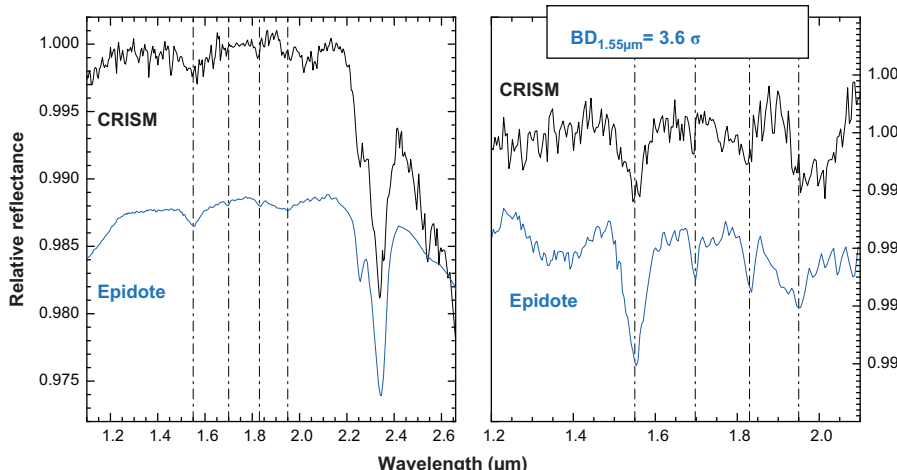


**Fig. 10.** Spectral rationale for the detection of epidote. The CRISM spectrum (left) is an average over five epidote end-members. The right frame is a continuum-removed close-up in the  $1.2$ – $2.1$   $\mu\text{m}$  region. The  $1.55$   $\mu\text{m}$  band unique to epidote is detected with a good confidence level ( $3.6\sigma$ ) while additional minor bands are tentatively detected at  $1.69$ ,  $1.83$  and  $1.95$   $\mu\text{m}$ .

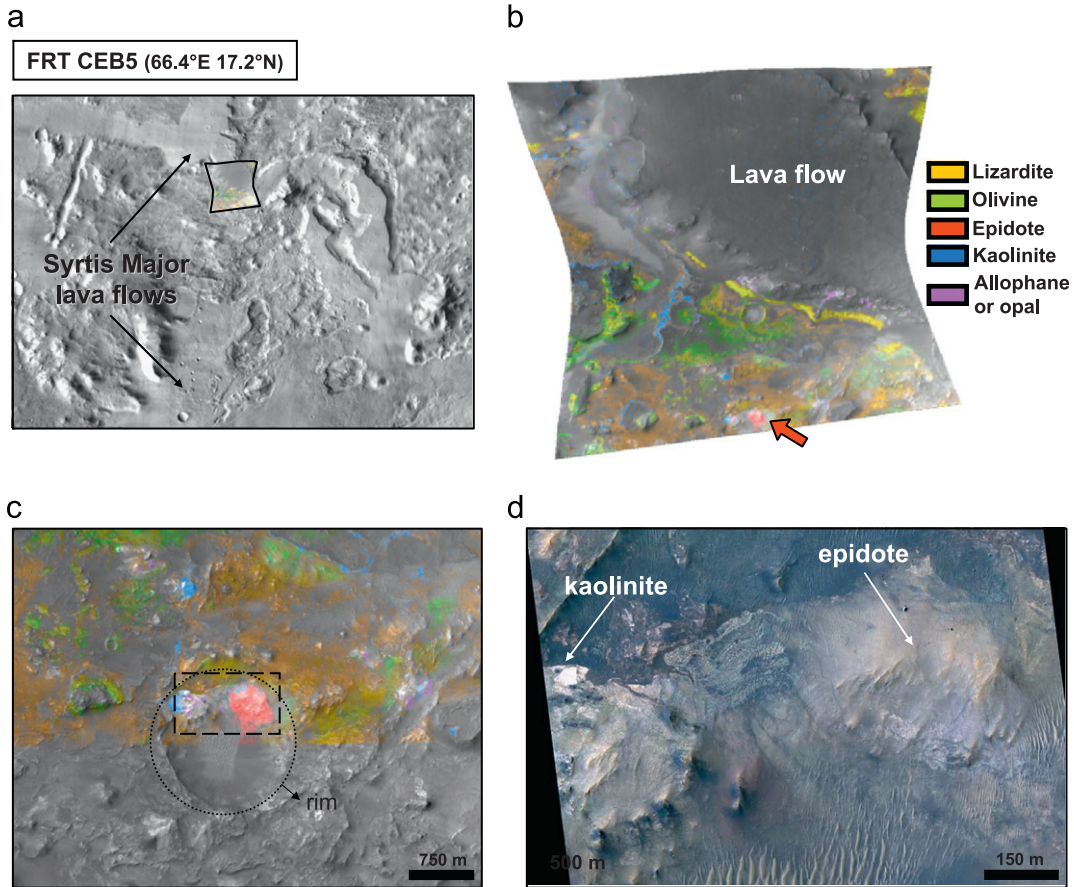


**Fig. 11.** Epidote detection at close proximity to Syrtis Major lava flows in S. Nili Fossae. (a) General context, the footprint of the CRISM observation is outlined. (b) CRISM mineral map showing the epidote signature in red to the South. (c) CTX close-up on the epidote outcrop on the rim of a 1 km wide rim-like circular structure. (d) HiRISE close-up on the epidote outcrop and a neighbouring kaolinite-bearing outcrop.

#FRT0000AD21,#FRT0000FBB). The impacts might have excavated deep metamorphic crustal material or more shallow hydrothermally altered lava flows. The presence of prehnite associated with epidote in these sites precludes formation at the surface, as prehnite forms metamorphically or hydrothermally only in the absence of CO<sub>2</sub> (Frey and Robinson, 1998; Ehlmann et al., 2009).

#### 4.3. Advantages and disadvantages

##### 4.3.1. A new spectral parameter: the 2.6 μm drop

In addition to diagnostic absorption bands, most hydrated minerals (phyllosilicates, sulphates, opaline silica) also exhibit a concave spectral shape in the 1–2.6 μm range. While the concavity in the 1–1.3 μm region is often modified by the presence of iron-bearing dust and/or olivine, the shape in the 2.1–2.6 μm region is less often biased. This shape, which is hard to study in the raw data as the continuum is dominated by the neutral mineralogy and photometric effects, can be investigated thanks to these new procedures. A new spectral parameter, which tests the presence of this concave feature, can be defined as

$$D_{2.6 \mu\text{m}} = 1 - \frac{\langle r(2.5-2.6 \mu\text{m}) \rangle}{\langle r(2.1-2.2 \mu\text{m}) \rangle}$$

We compare in Fig. 12 the mineral maps on a CRISM observation based on the BD1.90 and the new D2.60 spectral parameters. The former is commonly used to detect hydrated minerals on Mars. Both maps are in broad agreement, showing that the hydrous mineralogy is well mapped using the D2.60 parameter.

The D2.60 parameter improves on the BD1.90 parameter. For example, the black circles are detections of kaolinite and chlorite which are detected in the D2.60 map but not in the BD1.90 map. The 1.9 μm band parameter is considered as the most obvious signature of the detection of hydrated minerals, but it is less relevant for detecting non-structural H<sub>2</sub>O-bearing hydrous minerals such as carbonates, kaolin clays, prehnite, chlorite or epidote. After verifying the signatures manually, we also find that the new 2.6 μm parameter has overall higher sensitivity and lower noise than the BD1.90 parameter.

Contrarily to the BD1.90, the choice of wavelengths for this parameter also makes it less prone to false-positives caused by strong mafic signatures (as marked by white arrows in Figs. 5 and 12). The BD1.90 was computed using the tie-points-based continuum removal which should tackle these contaminants. Despite this, a residual false-positive is present (white arrow) and is due to the presence of very strong localized mafic (dunite) signatures. The bottom map uses the D2.60 parameter without the tie-points continuum removal and is not affected by this false positive.

One drawback however is its sensitivity to water frost which needs to be masked out using the ice spectral parameter.

##### 4.3.2. Optional atmospheric correction

Another benefit of this method is that it renders the atmospheric correction non-mandatory. If the atmospheric gas and aerosol opacity is homogeneous within the field of view, it is removed alongside other systematic biases. Very similar maps and spectra are generated based on the processed cubes both

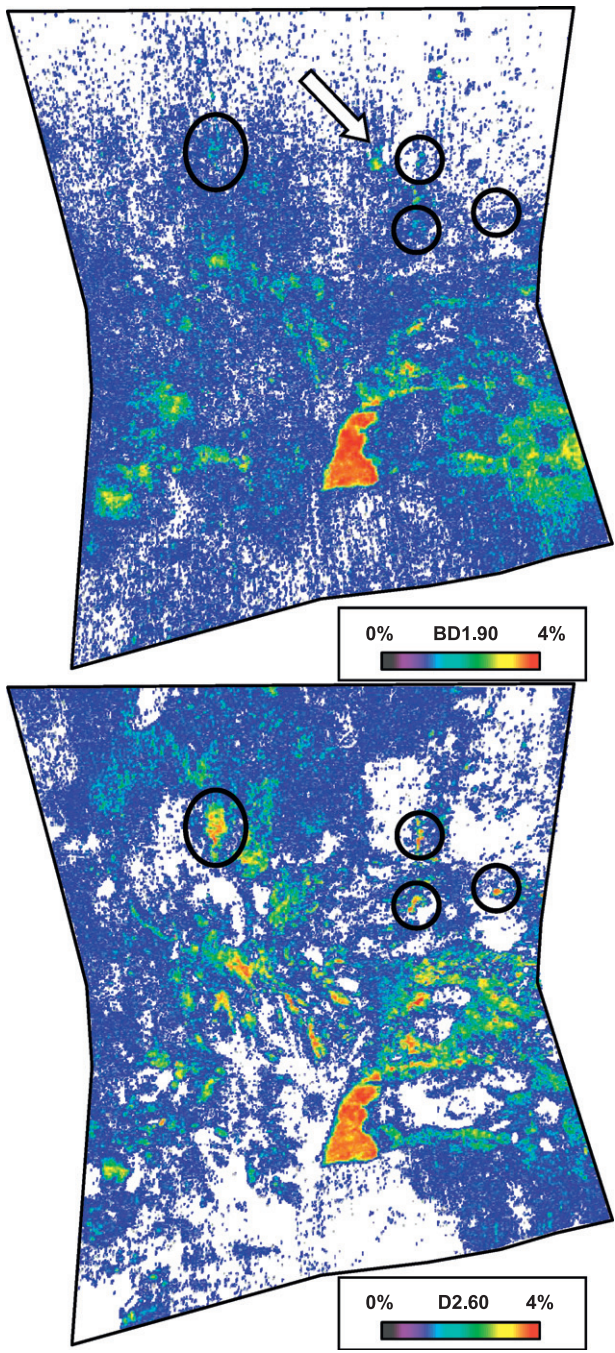


**Fig. 12.** New spectral parameter D2.60 (2.5–2.6  $\mu\text{m}$  drop). The top map uses the BD1.90 parameter commonly used to detect all hydrated minerals. The cube is processed using all the above steps, including the tie-points-based continuum removal to reduce contaminations by strong mafic signatures. The bottom map shows the new D2.60 parameter map.

corrected and un-corrected for atmospheric gas absorptions. In practice, however, since the gimbal imposes varying along-track emergence (and phase) angles and thus atmospheric opacity, an atmospheric correction prior to the removal of the neutral mineralogy is recommended to reduce artefacts in the 1.9  $\mu\text{m}$  region.

#### 4.3.3. Computational speed and reduced dimensionality

Our data reduction scheme is optimized for reducing the computational time. The use of simple and robust algorithms

allows a considerable gain in time when compared to the standard processing pipeline from the CAT CRISM toolkit (available on the PDS node). A standard data reduction from I/F to surface reflectance followed by linear continuum removal and running a standard set of spectral parameter is  $\sim 2.9$  faster than the CAT pipeline, excluding manual interventions in CAT which are removed altogether with this method (which batch processes a list of CRISM observations). The gain in time for processing the entire dataset ( $> 15\,000$  targeted observations) is considerable.

Downlink transfer rates to Earth are a critical part of any planetary mission. Adapting this procedure to run on on-board computers with sufficient processing power could prove valuable in tackling this issue. Each observation could be screened for interesting mineralogy with only very little data actually down-linked for evaluation (an estimated 450 times less data than the full observation in the case of CRISM). The full observation would then be retrieved if these browse products proved promising. This could be useful in particular to instruments performing reconnaissance of landing sites such as VIRTIS/Rosetta or landed instruments such as MicrOmega.

#### 4.3.4. Limitation

There are two main limitations. First, the accuracy of the identification of individual mineral classes which is about 60% compared to a manual investigation. This is a limitation of the spectral parameter method and should pose less of a problem if the method is applied to planetary surfaces with a lower spectral variance or when searching for minerals with broader bands. Second, this method is not well adapted for large mineral exposures that cover near to all the extent of the field of view, as they would be treated as systematic minerals and partly removed. This is the case on Mars in select regions and while the band depths may be under-estimated, the method does not remove the signatures altogether.

## 5. Conclusions

We developed a pipeline to batch process hyperspectral observations in the prospect of extracting weak mineral signatures, which we successfully applied to CRISM observations of hydrated minerals on Mars. Simple processing steps are introduced to tackle generic instrument artefacts and to remove the neutral spectral components in the spectra. By an appropriate combination of spectral parameters, we derive spectral end-members which assess the spectral diversity of any observation. These end-members are extracted using spectral stacking and automatically fitted to laboratory spectra. The pipeline yields a reduced-dimensionality set of spectral end-members with potential laboratory matches and mineral maps regrouped in a browse product for rapid viewing.

The 11 end-members used with CRISM successfully extracted minerals that encompass the entire hydrated mineral diversity found to-date on Mars. The use of simple algorithms allows reduction of the processing time compared to the standard CRISM CAT pipeline while providing accurate results and is more appropriate for screening large datasets. This method has led to the discovery of a new hydrated mineral on Mars, epidote. Large-scale evaluation in the northern Hellas province demonstrates that this method can perform a rapid assessment of the mineral potential of a CRISM observation with very high accuracy ( $> 90\%$ ). A thorough manual investigation remains paramount however. Further discrimination of the hydrated minerals can also be done at lower accuracy ( $\sim 60\%$ ). This is mainly due to the presence of transient artefacts, residual ice and bad atmospheric correction contaminating the 1.9–2.2  $\mu\text{m}$  bands. Better filtering of these

sources of error through additional spectral parameter combinations should provide more accurate end-members.

The pipeline is IDL-based and reads PDS-formatted CRISM file formats and can be adapted to generic datasets. It is available upon request.

## References

- Balan, E., Saitta, A.M., Mauri, F., Lemaire, C., Guyot, F., 2002. First-principles calculation of the infrared spectrum of lizardite. *American Mineralogist* 87, 1286–1290. <<http://ammin.geoscienceworld.org/cgi/reprint/87/10/1286.pdf>>.
- Bibring, J.P., Langevin, Y., Mustard, J.F., Poulet, F., Arvidson, R., Gendrin, A., Gondet, B., Mangold, N., Pinet, P., Forget, F., 2006. Global mineralogical and aqueous Mars history derived from OMEGA/Mars express data. *Science* 312, 400–404.
- Bishop, J., Lane, M., Dyr, M., Brown, A., 2008. Reflectance and emission spectroscopy study of four groups of phyllosilicates: smectites, kaolinite–serpentines, chlorites and micas. *Clay Minerals* 43, 35–54.
- Brown, R.H., Soderblom, L.A., Soderblom, J.M., Clark, R.N., Jaumann, R., Barnes, J.W., Sotin, C., Buratti, B., Baines, K.H., Nicholson, P.D., 2008. The identification of liquid ethane in Titan's Ontario Lacus. *Nature* 454, 607–610.
- Carter, J., Poulet, F., Ody, A., Bibring, J.P., Murchie, S., 2011. Global distribution, composition and setting of hydrous minerals on mars: a reappraisal In: Lunar and Planetary Institute Science Conference Abstracts, p. 2593.
- Carter, J., Poulet, F., Bibring, J.-P., Mangold, N., Murchie, S. L. Hydrous minerals on Mars as seen by the CRISM and OMEGA imaging spectrometers: updated global view. *J. Geophys. Res.* <http://dx.doi.org/10.1029/2012JE004145>, in press.
- Clark, R., 2007. USGS Digital Spectral Library spilib06a: U.S. Geological Survey, Digital Data Series 231, <<http://speclab.cr.usgs.gov/spectral.lib06>>.
- Clark, R.N., King, T.V., Klejwa, M., Swayne, G.A., Vergo, N., 1990. High spectral resolution reflectance spectroscopy of minerals. *Journal of Geophysical Research* 95, 12653–12680.
- Clark, R.N., Roush, T.L., 1984. Reflectance spectroscopy—quantitative analysis techniques for remote sensing applications. *Journal of Geophysical Research* 89, 6329–6340.
- Dole, H., Lagache, G., Puget, J., Caputi, K.I., Fernández-Conde, N., Le Floc'h, E., Papovich, C., Pérez-González, P.G., Rieke, G.H., Blaylock, M., 2006. The cosmic infrared background resolved by Spitzer. Contributions of mid-infrared galaxies to the far-infrared background. *Astronomy and Astrophysics* 451, 417–429 arXiv:astro-ph/0603208.
- Ehlmann, B.L., Mustard, J.F., Murchie, S.L., Bibring, J.P., Meunier, A., Fraeman, A.A., Langevin, Y., 2011. Subsurface water and clay mineral formation during the early history of Mars. *Nature* 479, 53–60.
- Ehlmann, B.L., Mustard, J.F., Swayne, G.A., Clark, R.N., Bishop, J.L., Poulet, F., Des Marais, D.J., Roach, L.H., Milliken, R.E., Wray, J.J., Barnouin-Jha, O., Murchie, S.L., 2009. Identification of hydrated silicate minerals on Mars using MRO-CRISM: geologic context near Nili Fossae and implications for aqueous alteration. *Journal of Geophysical Research (Planets)* 114, E00D08.
- Erard, S., Calvin, W., 1997. New composite spectra of mars, 0.4–5.7 μm. *Icarus* 130, 449–460.
- Frey, M., Robinson, D., 1998. Low-Grade Metamorphism. Wiley-Blackwell.
- Gilmore, M.S., Thompson, D.R., Anderson, L.J., Karamzadeh, N., Mandrake, L., Castaño, R., 2011. Superpixel segmentation for analysis of hyperspectral data sets, with application to Compact Reconnaissance Imaging Spectrometer for Mars data, Moon Mineralogy Mapper data, and Ariadnes Chaos, Mars. *Journal of Geophysical Research (Planets)* 116, E07001.
- Golombek, M., Grant, J., Kipp, D., Vasavada, A., Kirk, R., Ferguson, R., Bellutta, P., Calef, F., Larsen, K., Katayama, Y., Huertas, A., Beyer, R., Chen, A., Parker, T., Pollard, B., Lee, S., Sun, Y., Hoover, R., Sladek, H., Grotzinger, J., Welch, R., Noe Dobrea, E., Michalski, J., Watkins, M., 2012. Selection of the Mars Science Laboratory Landing Site, *Space Science Reviews* 170, 641–737.
- Johnson, J.R., Grundy, W.M., Lemmon, M.T., Bell, J.F., Johnson, M.J., Deen, R.G., Arvidson, R.E., Farrand, W.H., Guinness, E.A., Hayes, A.G., Herkenhoff, K.E., Seelos, F., Soderblom, J., Squyres, S., 2006. Spectrophotometric properties of materials observed by Pancam on the Mars Exploration Rovers: 1. Spirit. *Journal of Geophysical Research (Planets)* 111, E02S14.
- Lounejeva, E., Elias-Herrera, M., Ortega-Gutiérrez, F., Cedillo-Pardo, E., 2003. Origin of epidote from the impact melt of the Chicxulub crater, Mexico. In: Dressler, B., Kenkemann, T., Schieber, M., Poessges, G. (Eds.), Large Meteorite Impacts, Abstract #4054.
- McCord, T.B., Hansen, G.B., Fanale, F.P., Carlson, R.W., Matson, D.L., Johnson, T.V., Smythe, W.D., Crowley, J.K., Martin, P.D., Ocampo, A., Hibbitts, C.A., Granahan, J.C., 1998. Salts on Europa's surface detected by Galileo's near infrared mapping spectrometer. *Science* 280, 1242.
- McGuire, P.C., Bishop, J.L., Brown, A.J., Fraeman, A.A., Marzo, G.A., Frank Morgan, M., Murchie, S.L., Mustard, J.F., Parente, M., Pelkey, S.M., Roush, T.L., Seelos, F.P., Smith, M.D., Wendt, L., Wolff, M.J., 2009. An improvement to the volcano-scan algorithm for atmospheric correction of CRISM and OMEGA spectral data. *Planetary and Space Science* 57, 809–815 0903.3672.
- Murchie, S., Arvidson, R., Bedini, P., Beisser, K., Bibring, J., Bishop, J., Boldt, J., Cavender, P., Choo, T., Clancy, R.T., Darlington, E.H., Des Marais, D., Espiritu, R., Fort, D., Green, R., Guinness, E., Hayes, J., Hash, C., Heffernan, K., Hemmler, J., Heyler, G., Humm, D., Hutcheson, J., Izenberg, N., Lee, R., Lees, J., Lohr, D., Malaret, E., Martin, T., McGovern, J.A., McGuire, P., Morris, R., Mustard, J., Pelkey, S., Rhodes, E., Robinson, M., Roush, T., Schaefer, E., Seagrave, G., Seelos, F., Silverglate, P., Slavney, S., Smith, M., Shyong, W.J., Strohbehn, K., Taylor, H., Thompson, P., Tossman, B., Wirzburger, M., Wolff, M., 2007. Compact reconnaissance imaging spectrometer for Mars (CRISM) on Mars reconnaissance orbiter (MRO). *Journal of Geophysical Research (Planets)* 112, E05S03.
- Murchie, S.L., Mustard, J.F., Ehlmann, B.L., Milliken, R.E., Bishop, J.L., McKeown, N.K., Noe Dobrea, E.Z., Seelos, F.P., Buczkowski, D.L., Wiseman, S.M., Arvidson, R.E., Wray, J.J., Swayne, G., Clark, R.N., Des Marais, D.J., McEwen, A.S., Bibring, J.P., 2009. A synthesis of Martian aqueous mineralogy after 1 Mars year of observations from the Mars Reconnaissance Orbiter. *Journal of Geophysical Research Planets* 114, E00D06.
- Mustard, J.F., Murchie, S.L., Pelkey, S.M., Ehlmann, B.L., Milliken, R.E., Grant, J.A., Bibring, J.P., Poulet, F., Bishop, J., Dobrea, E.N., Roach, L., Seelos, F., Arvidson, R.E., Wiseman, S., Green, R., Hash, C., Humm, D., Malaret, E., McGovern, J.A., Seelos, K., Clancy, T., Clark, R., Marais, D.D., Izenberg, N., Knudson, A., Langevin, Y., Martin, T., McGuire, P., Morris, R., Robinson, M., Roush, T., Smith, M., Swayne, G., Taylor, H., Titus, T., Wolff, M., 2008. Hydrated silicate minerals on Mars observed by the Mars Reconnaissance Orbiter CRISM instrument. *Nature* 454, 305–309.
- Parente, M., Mustard, J.F., Murchie, S., Seelos, F.P., 2011. Summarizing the spectral variability of CRISM images with endmember extraction. In: Lunar and Planetary Institute Science Conference, Abstract #2622.
- Pelkey, S.M., Mustard, J.F., Murchie, S., Clancy, R.T., Wolff, M., Smith, M., Milliken, R., Bibring, J.P., Gendrin, A., Poulet, F., Langevin, Y., Gondet, B., 2007. CRISM multispectral summary products: parameterizing mineral diversity on Mars from reflectance. *Journal of Geophysical Research Planets* 112, E08S14.
- Pieters, C., 2010. Reflectance Experiment Laboratory (relab), <<http://www.planetary.brown.edu/relab/>>.
- Poulet, F., Beatty, D.W., Bibring, J.P., Bish, D., Bishop, J.L., Noe Dobrea, E., Mustard, J.F., Petit, S., Roach, L.H., 2009. Key scientific questions and key investigations from the first international conference on martian phyllosilicates. *Astrobiology*, 9, 257–267.
- Poulet, F., Bibring, J.P., Mustard, J.F., Gendrin, A., Mangold, N., Langevin, Y., Arvidson, R.E., Gondet, B., Gomez, C., 2005. Phyllosilicates on Mars and implications for early martian climate. *Nature* 438, 623–627.
- Poulet, F., Gomez, C., Bibring, J., Langevin, Y., Gondet, B., Pinet, P., Bellucci, G., Mustard, J., 2007. Martian surface mineralogy from Observatoire pour la Minéralogie, l'Eau, les Glaces et l'Activité on board the Mars Express spacecraft (OMEGA/MEx): Global mineral maps. *Journal of Geophysical Research Planets* 112, E08S02.
- Poulet, F., Mangold, N., Loizeau, D., Bibring, J., Langevin, Y., Michalski, J., Gondet, B., 2008. Abundance of minerals in the phyllosilicate-rich units on Mars. *Astronomy and Astrophysics* 487, L41–L44.
- Seelos, F.P., Murchie, S.L., Humm, D.C., Barnouin, O.S., Morgan, F., Taylor, H.W., Hash, C., Crism Team, 2011. CRISM data processing and analysis products update calibration, correction, and visualization. In: Lunar and Planetary Institute Science Conference, Abstract #1438.
- Seelos, F.P., Parente, M., Clark, T., Morgan, F., Barnouin-Jha, O.S., McGovern, A., Murchie, S.L., Taylor, H., 2009. CRISM hyperspectral data filtering with application to MSL landing site selection. *AGU Fall Meeting Abstracts* A1234+.
- Vincendon, M., 2008. Modélisation du transfert radiatif dans l'atmosphère martienne pour la détermination des propriétés spectrales de surface et la caractérisation des aerosols martiens à partir des données OMEGA. Ph.D. Thesis. Institut d'Astrophysique Spatiale.
- Vincendon, M., Langevin, Y., Poulet, F., Pommerol, A., Wolff, M., Bibring, J.P., Gondet, B., Jouget, D., 2009. Yearly and seasonal variations of low albedo surfaces on Mars in the OMEGA/MEx dataset: constraints on aerosols properties and dust deposits. *Icarus* 200, 395–405 1103.3426.